LIMNOLOGY and OCEANOGRAPHY: METHODS

ASLO

Limnol. Oceanogr.: Methods 20, 2022, 146–158

doi: 10.1002/lom3.10477

Commercially available unoccupied aerial systems for monitoring harmful algal blooms: A comparative study

Edna G. Fernandez-Figueroa [1,2]* **Alan E. Wilson** [1] **Stephanie R. Rogers** [2]

[1]School of Fisheries, Aquaculture, and Aquatic Sciences, Auburn University, Auburn, Alabama
[2]Department of Geosciences, Auburn University, Auburn, Alabama

Abstract

Reliable remote sensing platforms and methods for monitoring phytoplankton are needed for mitigating the detrimental impacts of cyanobacterial harmful algal blooms on small inland waterbodies. Commercial unoccupied aerial systems (UASs) present an affordable high-resolution solution for the rapid assessment of cyanobacterial abundance in small aquatic systems by recording the reflectance of photosynthetic pigments found in all phytoplankton (i.e., chlorophyll *a* [Chl *a*]) and those related to cyanobacteria (i.e., phycocyanin). This study evaluates the performance of four sensors, including visible light spectra (red, green, blue - [RGB]) sensors on the Phantom 4 and Phantom 4 Professional platforms, the MAPIR Survey3W modified multispectral (i.e., near-infrared, green, blue) sensor, and the Parrott Sequoia multispectral (i.e., green, red, near-infrared, red-edge) sensor for estimating cyanobacterial abundance. The performance of each sensor was determined by comparing 26 vegetation indices to Chl *a* and phycocyanin measurements of 54 ponds that varied in size and productivity. Vegetation indices that included the red and near-infrared wavelengths generated from Parrot Sequoia aerial images provided the best Chl *a* (i.e., Normalized Difference Vegetation Index, $r^2 = 0.79$, $p < 0.0001$) and phycocyanin (i.e., Green Normalized Difference Vegetation Index, $r^2 = 0.64$, $p < 0.0001$) estimates. The RGB sensors were moderately effective for estimating Chl *a*, whereas the MAPIR Survey3W generated poor estimates of both pigments due to differences in recorded wavelengths. Results suggest commercial multiband multispectral UAS sensors provide a low-cost, plug-and-play alternative for managers and researchers interested in integrating remote sensing tools for quantitatively estimating phytoplankton abundance in small inland systems.

Small inland waterbodies are ubiquitous and provide important ecosystems services, including, but not limited to, drinking water supply, food production, aquatic recreation, and climate regulation (Biggs et al. 2017). Blooms dominated by cyanobacterial harmful algal blooms (CyanoHABs) are becoming more frequent and intense as a result of climate change and cultural eutrophication (Huisman et al. 2018). CyanoHABs impair freshwater systems through the production of toxins (i.e., cyanotoxins) linked to illness and fatalities in livestock, pets, and humans, as well as off-flavor compounds (e.g., geosmin and 2-methylisoborneol) that impart a musty scent and flavor on drinking water and farm-raised fish leading to significant economic losses to aquaculture and drinking water industries (Merel et al. 2013; Tucker and Schrader 2020). CyanoHABs are traditionally monitored via cell counts or by measuring the concentration of photosynthetic pigments found in all phytoplankton (i.e., chlorophyll *a* [Chl *a*]) relative to accessory pigments abundant in cyanobacteria (i.e., phycocyanin). However, traditional methods are constrained by processing times, training, cost, and may not be representative of the entire waterbody (Kutser 2004; Merel et al. 2013). Reliable tools that can rapidly and accurately quantify the abundance of ecologically important phytoplankton (e.g., green algae and diatoms) relative to toxin-producing cyanobacteria in small drinking water sources, aquaculture farms, and recreational water bodies are necessary for implementing monitoring, response, and forecasting tools for mitigating the ecological, economic, and health impacts of CyanoHABs.

In large inland systems, satellite remote sensing has been useful for recording long-term and seasonal bloom dynamics and understanding how external factors, such as surface water temperature, meteorological events, and anthropogenic nutrient loading drive CyanoHAB occurrence (Wynne et al. 2010; Shi et al. 2017). Several satellites generate reliable data for

*Correspondence: egf0013@auburn.edu

Additional Supporting Information may be found in the online version of this article.

monitoring the spatial and temporal distribution of algal blooms, including satellites from the Landsat series, Moderate Resolution Imaging Spectroradiometer (MODIS) Aqua and Terra, MEdium Resolution Imaging Spectrometer (MERIS), Sentinel 2-A/B, and Hyperion (Brivio et al. 2001; Kutser 2004; Kutser et al. 2006; Yacobi et al. 2011; Shi et al. 2017; Drozd et al. 2020). Yet, low spatial and temporal resolution, atmospheric correction challenges, cloud cover, slow data-product turn-around times, and cost of some satellite products can limit the application of satellite remote sensors for monitoring CyanoHABs in small inland systems (Lomax et al. 2005). For example, MERIS is a multispectral sensor used to detect and measure cyanobacteria when present at high densities (Kutser et al. 2006; Wynne et al. 2010). However, the spatial resolution of 300 m and revisit times of 2 days limit its application for smaller waterbodies. The hyperspectral imager in space, Hyperion, collects data from 196 spectral bands in the 400–2500 nm region. Although Hyperion data have been useful for monitoring water quality parameters, such as Chl *a* and chromophoric dissolved organic matter (Brando and Dekker 2003), it's 30 m spatial resolution is not sufficient for studying inland CyanoHABs, particularly in the presence of patchy surface scums (Kutser 2004). Therefore, satellite data are not reliable when monitoring small inland systems, such as ponds, lakes, and rivers, especially if cyanobacteria are present.

Unoccupied aerial systems (UASs) (remotely piloted remote sensing platforms; i.e., drones), show great potential for bridging the gap between *in situ* water sampling and satellite remote sensing. UASs collect high-resolution aerial data with minimal atmospheric disturbance from cloud coverage, allow flexible flight planning with rapid turn-around times, and are available in a variety of wavelength combinations (Kislik et al. 2018). However, UASs are restricted by battery life that can limit flight times, maximum payload capabilities that determine which sensors and communication hardware can be mounted on the aircraft, weather limitations (e.g., wind and precipitation), GPS connection needs, and startup costs (Kislik et al. 2018). Moreover, factors such as sun glint, shadows, suspended solids, and water depth can cause inaccurate phytoplankton estimates or complicate image processing for both satellite and UAS remote sensing (Kislik et al. 2018). Commercially available UAS sensors are classified as visible wavelength (RGB), modified or multiband multispectral, thermal, or hyperspectral. Multispectral sensors record wavelengths that fall within and outside the visible light spectrum (i.e., RGB and near-infrared, respectively) and are classified as multiband or modified. Multiband multispectral sensors collect data for 4–6 bands, and each band typically has a dedicated sensor. While more expensive, multiband sensors generate high-resolution results, and many are designed to measure the photosynthetic activity of terrestrial crops. For example, the Parrot Sequoia multiband multispectral sensor records green, red, red-edge, and near-infrared bands, which can be used to calculate the Normalized Difference Vegetation Index (NDVI) and is marketed for measuring crop health (Fig. 1). Sensors that measure the red-edge (735 nm) region of high reflectance between the red and near-infrared wavelengths can be as effective at estimating the Chl *a* concentration of crops as hyperspectral sensors (Lu et al. 2019). However, the value of the red-edge wavelength for monitoring CyanoHABs can be dependent on the trophic status of the waterbody (Cillero Castro et al. 2020). Modified multispectral sensors are a low-cost alternative to multiband multispectral sensors. One such example is the MAPIR Survey3W near-infrared, green, blue (NGB), which is an RGB sensor with a filter that sacrifices the red wavelength to record the near-infrared wavelength (Fig. 1). Although modified multispectral sensors typically have lower resolutions than multiband multispectral sensors, they have been used to estimate cyanobacterial buoyant packed cell volume (Van der Merwe and Price 2015). Lastly, many UASs, such as the DJI Phantom series, are equipped with an integrated RGB sensor that provides a cost-effective alternative to multispectral sensors (Fig. 1). RGB sensors can detect algal cover and biomass in coastal systems (Xu et al. 2018; Cheng et al. 2020), but further research is needed before these sensors can reliably estimate cyanobacterial abundance.

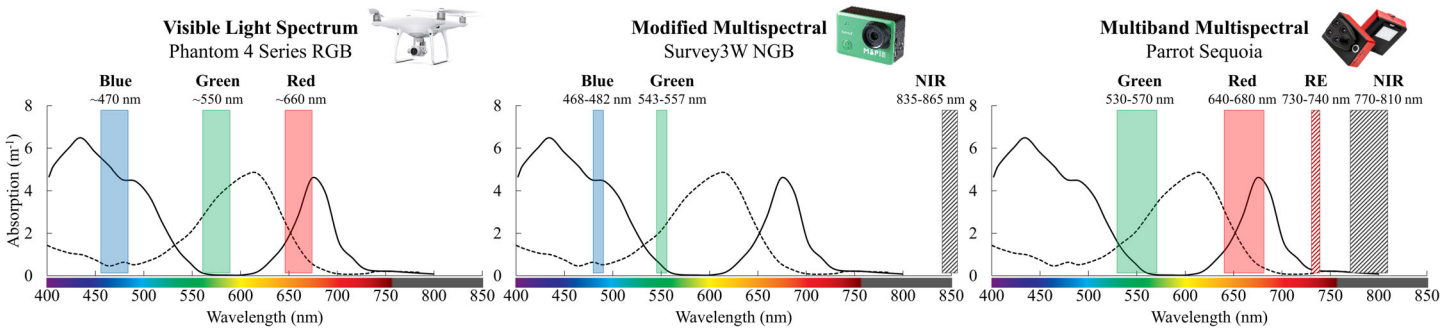

Fig 1. Measured wavelength (nm) for the DJI Phantom 4 and Phantom 4 Pro integrated RGB cameras, MAPIR Survey3W NGB modified 3-band multispectral sensors, and Parrot Sequoia multiband multispectral sensors utilized in this study, overlaid over the *in vivo* spectral absorption of Chl *a* (solid line) and phycocyanin (dashed line). Phantom 4 and Phantom 4 Pro series measured wavelengths are proprietary information and are therefore estimated from García-Fernández et al. (2021). Chlorophyll and phycocyanin spectral response curves are modified from Simis and Kauko (2012).

Monitoring CyanoHABs with UASs has been hindered by the lack of standardized methods for aerial image collection, validation techniques, and universal algorithms for processing UAS data (Kislik et al. 2018). In addition, there is no consensus on which sensor type or vegetation index works best for estimating Chl *a*, and few have been used to estimate phycocyanin concentration. Chl *a*, present in all phytoplankton, including chlorophytes and cyanobacteria, absorbs red and blue wavelengths at approximately 430 and 662 nm, respectively, and reflects green and near-infrared wavelengths at approximately 500 and 700–1300 nm, respectively (Fig. 1). Accessory pigments found in cyanobacteria, such as phycocyanin (absorbance at 620 nm), allow cyanobacteria to absorb light at a broader spectrum and protect them from solar radiation (Oliver et al. 2012). Additional factors, such as inorganic suspended matter, colored dissolved organic matter, and non-algal organic matter affect water reflectance properties, and these effects vary greatly based on the composition of the particles (Morel 2001). The absorbance and reflection characteristics of Chl *a* and phycocyanin can be magnified by calculating band ratio algorithms (i.e., vegetation indices) that emphasize the spectral characteristics of photosynthetic pigments, water, and soil leading to better estimates than single-band measurements (Xue and Su 2017). The goal of this study was to evaluate whether commercially available sensors are a feasible monitoring alternative for drinking water and aquaculture facility managers, as well as for researchers focused on smaller aquatic ecosystems. To determine which sensor and vegetation index combination is best for monitoring Chl *a* and phycocyanin, aerial images collected by four sensors that vary in measured wavelengths, bandwidths, resolution, and price were used to calculate 26 vegetation indices. The four sensors chosen are commonly used for agricultural research and include two visible RGB sensors (DJI Phantom 4 and Phantom 4 Pro), one modified multispectral sensor (MAPIR Survey3W), and a multiband multispectral sensor (Parrot Sequoia). Vegetation index values were compared to *in situ* Chl *a* and phycocyanin measurements to determine which sensor and vegetation index combination should be considered for estimating phytoplankton and cyanobacterial abundance in small aquatic systems.

Materials and procedures

Study area and field survey methods

Aerial images were collected over several research, aquaculture, and recreational ponds from September 2019 to July 2020 (Table 1). UAS flights 1, 2, and 3 were conducted at a commercial aquaculture facility in Alabama, USA (Fig. 2). UAS flights 4, 5, 6, and 7 were conducted at the E.W. Shell Fisheries Center of Auburn University in Auburn, Alabama, USA, which is a 1600-acre research facility equipped with over 300 man-made experimental aquaculture ponds ranging in size, depth, and productivity (Fig. 3). Research and commercial aquaculture ponds frequently experience high cyanobacterial

Table 1. UAS flight details for this study. Vertical and horizontal accuracy of each flight is 1–3× GSD. GSD values correspond to both aerial images and finished orthomosaics. Image % overlap refers to front and side overlap.

Flight ID	1	2	3	4	5	6	7	8	9	10
Figure	2a	2b	2c	3a	3b	3d	3c	4a	4b	4c
Date	20 Nov 2019	14 Apr 2020	14 Apr 2020	03 Sep 2019	21 Feb 2020	18 Jun 2020	17 Jul 2020	17 Mar 2020	31 May 2020	10 Jul 2020
Time	11 : 30	10 : 40	14 : 01	8 : 45	16 : 00	8 : 00	9 : 00	16 : 00	10 : 40	8: 40
Location	AF	AF	AF	RF	RF	RF	RF	AP	AP	AP
Latitude	32.390	32.413	32.396	32.662	32.662	32.654	32.662	32.588	32.588	32.588
Longitude	−87.349	−87.375	−87.367	−85.496	−85.496	−85.488	−85.496	−85.484	−85.484	−85.484
Flight altitude (m)	75	75	75	50	50	30	50	50	50	75
GSD (cm/px)	3.28	2.05	3.28	1.36	2.23	1.31	2.19	2.19	2.19	2.19
Image % overlap	75	75	75	80	75	75	75	75	75	75
Flight dimensions (m)	485 × 469	924 × 942	358 × 816	161 × 305	114 × 196	63 × 102	166 × 297	147 × 195	147 × 195	147 × 195
Wind (mph)	7	8	12	5	7	0	0	1	5	0
Humidity	37%	60%	57%	69%	54%	78%	72%	60%	49%	79%
Sites	7	8	5	5	16	1	19	1	1	1
Water samples	10	8	6	5	16	1	19	2	1	2

GSD, ground sampling distance; AF, aquaculture facility; RF, research facility; AP, aesthetic pond.

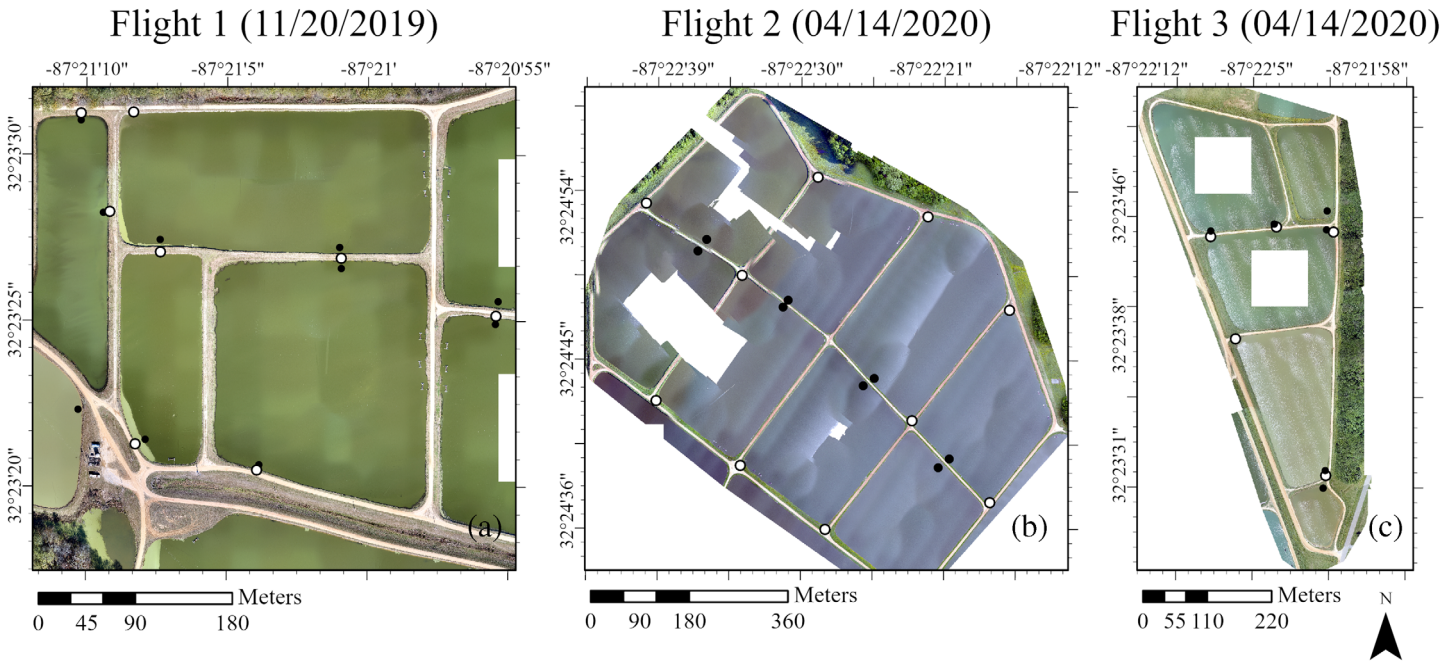

Fig 2. Orthomosaics generated from aerial images collected with the integrated RGB sensor of a Phantom 4 Pro at a commercial aquaculture facility in Alabama, USA. Water sample collection locations are shown as black dots and GCP locations are shown as white dots. Panel labels (a-c) correspond with columns in Table 1. White blocks seen in (**b**) and (**c**) are caused by orthomosaic generation failure due to wind gusts that caused the aircraft to drift from the pre-specified flight path.

abundance due to long residence times and high nutrient inputs in the form of fish feed. Flights 8, 9, and 10 were conducted over the man-made aesthetic pond at the Jule Collins Smith Museum of Fine Art at Auburn University, which frequently experiences dense cyanobacterial blooms (Fig. 4).

Aerial images were collected on clear days when the solar altitude was less than 43° to avoid sun glint effects (Ortega-Terol et al. 2017). Flights were fully automated based on specified flight plans on the free mobile device application Pix4Dcapture. Details for each flight are found in Table 1. Ground control targets (black and gray, 0.37 m^2) were positioned around the survey area prior to flights as horizontal ground control points (GCP). Geographic coordinates were collected for each GCP target and each water sample collection site using a Trimble Geo7x Handheld GNSS System. Geographical point data were then post-processed with the Global Navigation Satellite System (GNSS) post-processing program Trimble GPS Pathfinder Office to improve geospatial accuracy during aerial image processing (±4 cm accuracy).

UAS description

Due to the weight of the modified and multiband multispectral sensors, two separate UASs were used (Table 2). Flights were conducted immediately one after the other to minimize sun angle variation between flights.

The MAPIR, Inc. Survey3W NGB modified 3-band multispectral sensor was mounted on a DJI Phantom 4 quadcopter. The Survey3W NGB is a Sony Exmor R IMX117 12MP (Bayer RGB) camera that sacrifices the red band to measure the near-infrared wavelength (Fig. 1; Table 2). The Survey3W was programmed to capture aerial images at a 0.5 s interval at nadir (90° in reference to the horizontal plane) and collect both RAW data (GPS location, 12 bit per channel) and JPEG images (8 bit per channel). The Survey3W was equipped with a Survey3 Advanced GPS Receiver (20.6 g) that generates a geolocation stamp for each JPEG image captured. The Survey3W was mounted on the Phantom 4 quadcopter using a plastic tilting camera mount in a way that did not obstruct the Phantom 4's RGB camera. Visual light spectrum reflectance data were collected with the Phantom 4's integrated visual spectrum 12.4 M RGB camera (Fig. 1). The Phantom 4 was equipped with a GPS/GLONASS integrated system that GPS tags the images with latitude, longitude, and altitude information (Table 2).

The Parrot Sequoia 4.0 multiband multispectral sensor was mounted on a DJI Phantom 4 Pro quadcopter. The Parrot Sequoia multispectral sensor is equipped with green, red, red-edge and near-infrared monochrome sensors, an RGB sensor and an integrated GPS and light sensor (Fig. 1; Table 2). Images were captured at a 1.5 s interval at nadir. The Parrot Sequoia was mounted on the Phantom 4 Pro using a plastic mount that did not block the field of view of the UAS's integrated RGB camera. Visual light spectrum images were collected at nadir with the Phantom 4 Pro's integrated 20 M RGB camera, and latitude, longitude, and altitude information were collected with the UAS's GPS/GLONASS (Table 2).

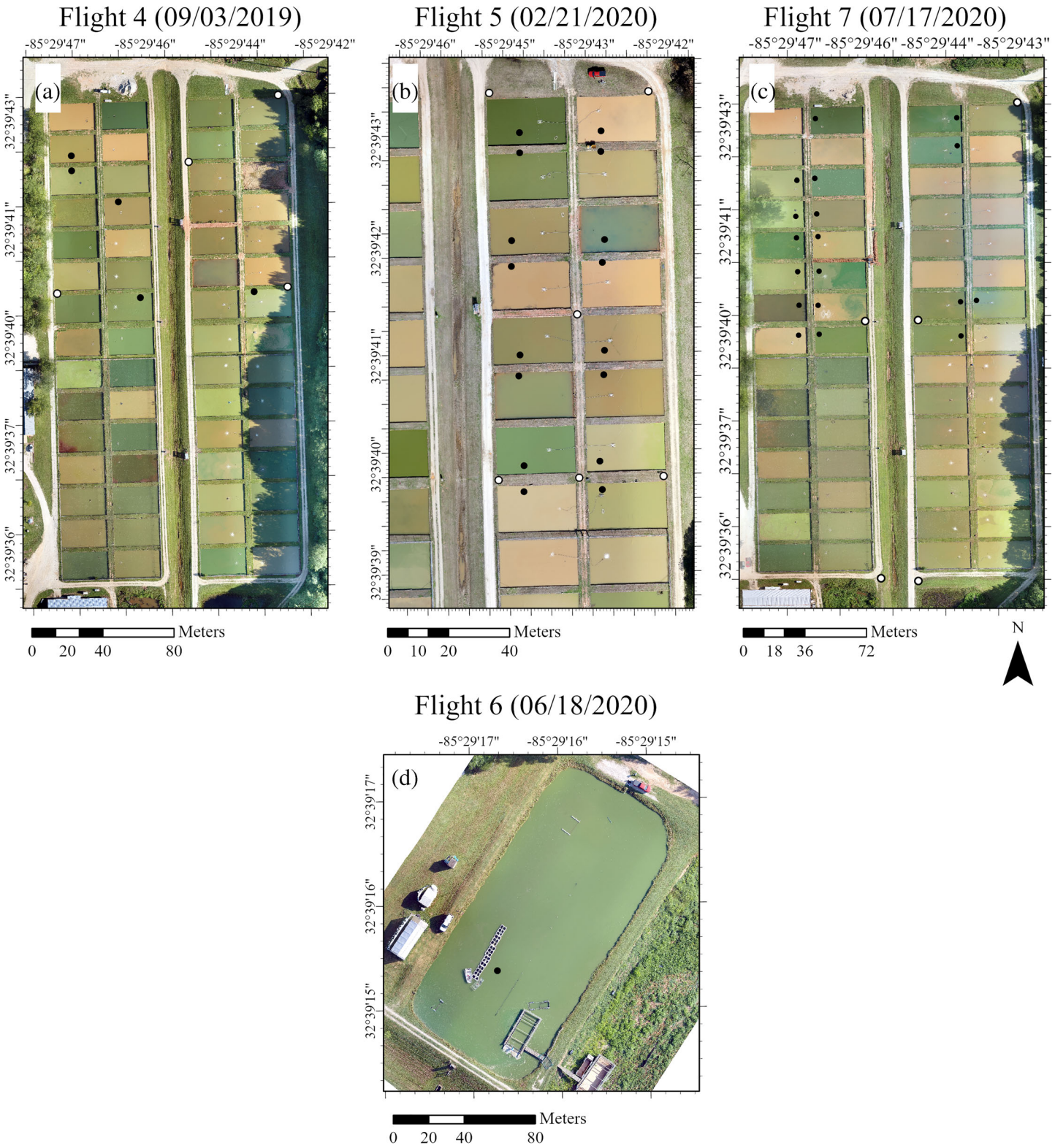

Fig 3. Orthomosaics generated from aerial images collected with the integrated RGB sensor of a Phantom 4 Pro at research ponds at Auburn University's E.W. Shell Fisheries Center. Panel labels (a-d) correspond with columns in Table 1. Water sample collection locations are shown as black dots and GCP locations are shown as white dots.

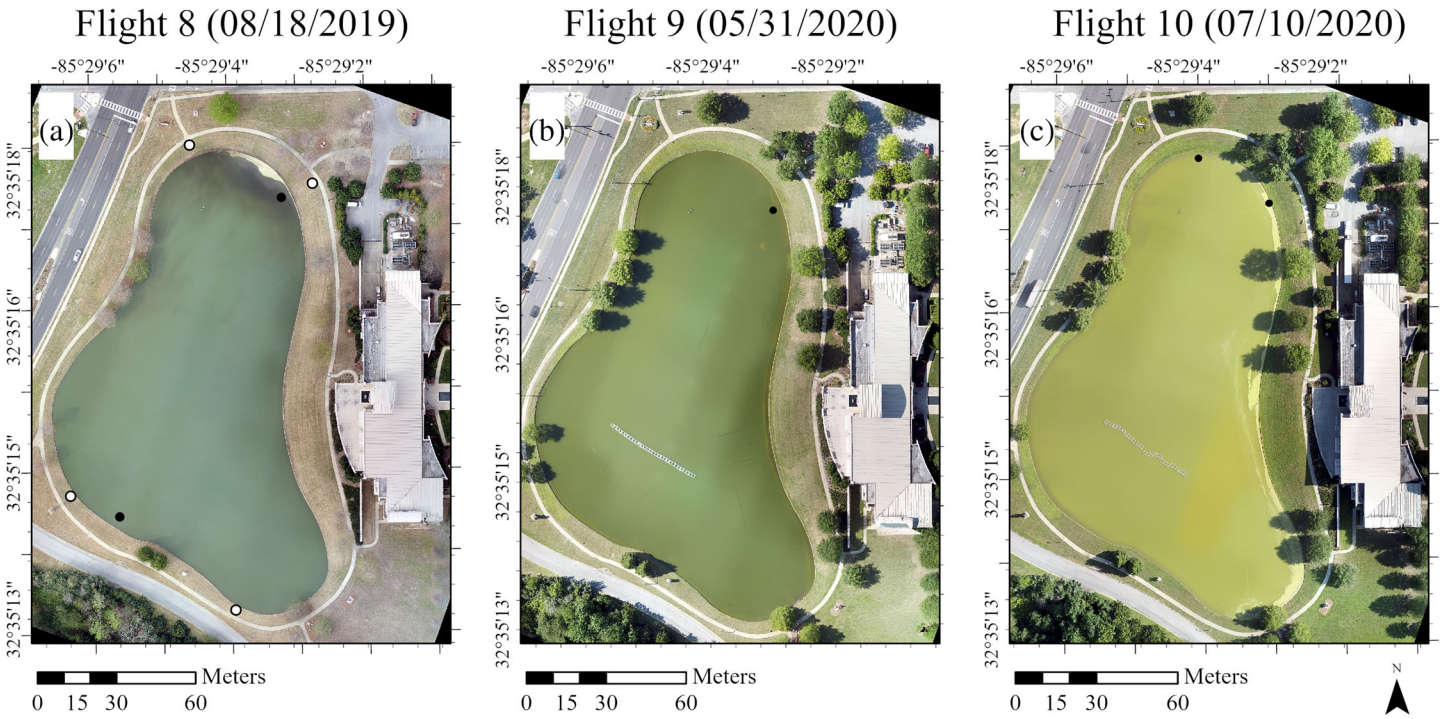

Fig 4. Orthomosaics generated from aerial images collected with the integrated RGB sensor of a Phantom 4 Pro at Auburn University's Jule Collins Smith Museum of Fine Arts pond. Panel labels (a-c correspond with columns in Table 1. Water sample collection locations are shown as black dots and GCP locations are shown as white dots. GCP data were not collected for flights 9 and 10.

Image processing

Prior to photogrammetric processing, Survey3W NGB JPEG images were combined with GPS-tagged RAW images using the MAPIR Camera Control software to create a TIFF file with all metadata included (MAPIR CAMERA 2020). Georeferenced Survey3W NGB images were then calibrated based on images of the MAPIR Calibration Target V2 collected immediately before and after UAS flights.

The Pix4Dmapper software was utilized for photogrammetric processing of the images from each sensor. A camera profile had to be added to Pix4Dmapper based on manufacturer specifications for the Survey3W NGB sensor. The Survey3W NGB, Phantom 4 RGB, and Phantom 4 Pro RGB cameras capture images by scanning the scene rapidly (i.e., rolling shutter), which often causes aerial image distortion or warping. To correct for rolling shutter effects, the rolling shutter correction setting was enabled for these sensors on the Pix4Dmapper software. The Parrot Sequoia monochrome sensors (multispectral) employ a global shutter, which captures the entire frame simultaneously; therefore, the rolling shutter correction was not necessary. GCP GPS data collected prior to flights were used to georeference images to improve spatial accuracy. Reflectance values for the Parrot Sequoia multispectral sensor were radiometrically calibrated based on images of the Parrot Sequoia radiometric calibration target collected immediately before and after UAS flights. Point cloud densification, digital surface models (DSM), orthomosaics, and reflection map generation for all the sensors were processed on Pix4Dmapper. Orthomosaics were generated by Pix4Dmapper by calculating the weighted average of the pixels in the original images. Calibrated orthomosaics for the four individual sensors were exported to ArcGIS Pro 2.6 for spectral calculations.

Post-processing was successful for most UAS flights, with the exception of flights 2 and 3. During these flights, incoming storms generated wind gusts that destabilized the aircraft causing it to tilt and shift from the pre-specified flight plan leading to image tie point generation failure in some areas and causing gaps in the final orthomosaic (Fig. 2). The orthomosaic from flight 3 has visible banding, which is due to solar reflection as this flight had to be postponed to later in the day due to inclement weather. Water samples were not collected from ponds that had visible shadows at the time of aerial flights and water sample collection, except for one pond in flight 4 (Fig. 3) that was partially affected by shadows in the opposite corner of the water sampling location.

Vegetation indices

The 26 vegetation indices (i.e., band ratio algorithms) calculated in this study are specified in Table 3. Vegetation index calculations were performed on ArcGIS Pro using the Raster

Table 2. Description of the two UASs utilized in this study. Each UAS composed of the unoccupied aerial vehicle (UAV) itself, as well as its integrated visible wavelength red, green, blue (RGB) camera, and onboard multispectral sensor.

	Modified multispectral UAS	Multiband multispectral UAS
UAV model	**DJI Phantom 4**	**DJI Phantom 4 Pro**
Type	Quadcopter	Quadcopter
Vertical position accuracy	± 0.5 m	± 0.5 m
Horizontal position accuracy	± 1.5 m	± 1.5 m
Max flight time	~ 28 min	~ 30 min
Max speed	20 m s^{-1}	45 m s^{-1}
Estimated payload capacity	~ 462 g	~ 462 g
Diagonal length	350 mm	350 mm
Weight with batteries	1380 g	1388 g
Retail value	$1500	$1500

RGB camera	**DJI Phantom 4 RGB**	**DJI Phantom 4 Pro RGB**
Field of view	94° 20 mm	84° 8.8 mm/24 mm
Image size	4000 × 3000 pixels	5472 × 3648 pixels
Spatial resolution	3.4 cm/pixel 80 m altitude	2.6 cm/pixel 80 m altitude
Effective pixels	12.4 M	20 M
Focal length	20 mm	24 mm

Onboard sensor	**MAPIR Survey3W**	**Parrot Sequoia**
Horizontal field of view	87° 19 mm	62°
Image size	4032 × 3024 pixels	1280 × 960 pixels
Spatial resolution	5.5 cm/pixel 120 m altitude	11 cm/pixel 120 m altitude
Focal length	3.37 mm	3.98 mm
Lens type	Non-fish eye	Non-fish eye
Weight	75.4 g	90 g
Dimensions	41 × 59 × 25 mm	75 × 59 × 3 mm
Retail value	$400	$3500

Calculator Tool by averaging the nine pixels around and including the sample location for each band of the calibrated orthomosaic for each sensor. Additional information regarding vegetation index development and original citations can be found in the Supporting Information Table S1.

Water sample collection and analyses

Seventy water samples were collected from 54 ponds that varied widely in their appearance, with some clear ponds and others containing suspended sediments, suspended algae, and/or thick cyanobacterial scum. The inclusion of clear and high sediment ponds was essential to ensure the sensors and vegetation indices were effective in a variety of systems, not just productive ponds. All ponds had mud substrates with limited benthic macrophyte cover, therefore noise caused by macrophyte Chl *a* was not considered in this study. Multiple water samples were collected and processed from several areas within larger ponds to account for spatial heterogeneity due to wind and aquaculture aerators pushing buoyant cyanobacteria to a localized section of the pond. All water samples were collected immediately after UAS flights to ensure they were representative of aerial images. Secchi depth (m) and physical water parameters, such as temperature, conductivity, and pH, were recorded using a handheld YSI ProDSS handheld multiparameter water quality meter. Water samples were collected using a rigid tube sample up to the Secchi depth of the sample site (average 16.11 cm; range 0–75 cm). Surface samples were collected from areas where the Secchi depth was <10 cm. A known volume of well-mixed samples was filtered through Pall A/E filters and stored frozen in the dark for later algal pigment extraction. Chl *a* samples were measured to estimate algal abundance using a Turner Designs Trilogy fluorometer with non-acidification chlorophyll module after a 24 h extraction in 90% aqueous ethanol in the dark at 4°C (Sartory and Grobbelaar 1984). Phycocyanin concentrations were measured to estimate cyanobacterial abundance using a Turner Designs Trilogy fluorometer with an orange module after grinding, extracting each filter in a 50 mM phosphate buffer in darkness for 4 h, centrifuging, and filtering (<0.2 μm) each sample (Kasinak et al. 2015). All water samples were run in duplicates and included blank controls.

Primary productivity varied among the ponds sampled (Supporting Information Table S2). Chl *a* concentrations ranged from 3 to 3090 $\mu g\ L^{-1}$ (average 293.49 $\mu g\ L^{-1}$) and phycocyanin concentrations ranged from 0 to 17,210 $\mu g\ L^{-1}$ (average 943.5 $\mu g\ L^{-1}$). High Chl *a* and phycocyanin concentrations are common in eutrophic and hypereutrophic systems, and some samples included a thick *Microcystis* sp. scum that was very dense, resulting in the extremely high pigment concentrations measured. Large ponds, such as the aesthetic pond sampled in flights 8–10 (Fig. 4), that contained surface scum were sampled from areas with and without scum to account for spatial variation within the pond. Samples from the same pond were treated individually; therefore, each sample represented a unique vegetation index value within the data set. Water samples were collected based on water transparency (measured as Secchi depth) to ensure the Chl *a* and phycocyanin samples represented the water column layer visible from aerial images.

Table 3. Vegetation indices calculated from DJI Phantom 4 and Phantom 4 Pro RGB sensors (RGB), MAPIR Survey3W NGB modified multispectral sensor (NGB), and Parrot Sequoia multiband multispectral sensor (multi) imagery.

Vegetation index	Formula	Sensor
2-Band Enhanced Vegetation Index (EVI2)	$2.5((NIR - R)/(NIR + 2.4 * R + 1))$	Multi
Blue Normalized Vegetation Index (BNDVI)	$(NIR - B)/(NIR + B)$	NGB
Color Index of Vegetation Extraction (CIVE)	$0.441 * R - 0.881 * G + 0.385 * B + 18.787$	RGB
Difference Vegetation Index (DVI)	$NIR - R$	Multi
Enhanced Normalized Difference Vegetation Index (ENDVI)	$((NIR + G) - (2 * B))/((NIR + G) + (2 * B))$	NGB
Excess Green Index (EXG)	$2 * G - R - B$	RGB
Excess Green Minus Excess Red (ExGR)	$ExG - 1.4\ R - G$	RGB
Green Chlorophyll Index (CiGreen)	$(NIR/G) - 1$	Multi and NGB
Green Normalized Difference Vegetation Index (GNDVI)	$(NIR - G)/(NIR + G)$	Multi and NGB
Green–Red Ratio Index (GRRI)	G/R	Multi and RGB
KIVU	$(B - R)/G$	RGB
Modified Simple Ratio Red-Edge (MSRre)	$(NIR/RE - 1)/\sqrt{(NIR/RE + 1)}$	Multi
Modified Single Ratio (MSR)	$(NIR/R) - 1/(\sqrt{NIR/R} + 1)$	Multi
Normalized Difference Red-Edge Index (NDRE)	$NIR - RE/NIR + RE$	Multi
Normalized Difference Vegetation Index (NDVI)	$(NIR - R)/(NIR + R)$	Multi
Normalized Difference Vegetation Structure Index (NDVSI)	$(NIR - [R + G]0.5)/(NIR + [R + G]\ 0.5)$	Multi
Normalized Green-Blue Difference Index (NGBDI)	$G - B/G + B$	NGB and RGB
Normalized Green-Red Difference Index (NGRDI)	$(G - R)/(G + R)$	Multi and RGB
Ratio Normalized Difference Vegetation Index (RNDVI)	$((NIR - R)/(NIR + R)) * NIR/R$	Multi
Ratio Vegetation Index (RVI or SR)	NIR/R	Multi
Red Green Blue Vegetation Index (RGBVI)	$G^2 - R \times B/G^2 + R \times B$	RGB
Red-Edge Chlorophyll Index (CiRedEdge)	$(NIR/RE) - 1$	Multi
Red-Green Ratio Index (RGRI)	R/G	Multi and RGB
Visible Atmospherically Resistant Index (VARIgreen)	$(G - R)/(G + R - B)$	RGB
Visible Band Difference VI (VDVI)	$(2 * G - R - B)/(2*G + R + B)$	RGB
Vegetativen (VEG)	$G/(R^a * B^{[1-a]})$, $a = 0.667$	RGB

B, blue; G, green; NIR, near-infrared; R, red; RE, red-edge.

Data analysis

Chl *a* and phycocyanin data were log-transformed (base 10) prior to statistical analysis to reduce heteroscedasticity that is common with water quality data that span large ranges. The linear relationship between the two pigments (Chl *a* and phycocyanin) and the vegetation index values generated from each sensor were determined by calculating Pearson correlations (significant relationship when $p < 0.05$; Schober et al. 2018). All statistical analyses were done using the *stats* package in the open-source statistical software RStudio (RStudio Inc., MA, USA).

Assessment

The four sensors and vegetation indices varied greatly in their ability to estimate total phytoplankton and cyanobacterial abundance (Tables 4 and 5; Supporting Information Fig. S1). RGB sensors on commercial UASs provide a cost-effective tool for monitoring photosynthetic activity. Despite differences in resolution, the 12.4 M Phantom 4 and 20 M Phantom 4 Pro RGB sensors generated similar vegetation index values for both Chl *a* and phycocyanin. Of the 12 vegetation indices calculated from the two RGB sensors, the Color Index of Vegetation Extraction (CIVE) generated the best estimates of Chl *a* concentration for the aerial images collected from the Phantom 4 ($r^2 = 0.31$, $p < 0.0001$) and Phantom 4 Pro ($r^2 = 0.35$, $p < 0.0001$; Table 4). CIVE was originally developed to differentiate between vegetation and soil to estimate crop growth without the need to measure near-infrared wavelengths (Kataoka et al. 2003), and it is not typically included in UAS aquatic ecosystem monitoring studies. Both RGB sensors were more sensitive to Chl *a* than phycocyanin. The Green–Red Ratio Index (GRRI) and Visible Atmospherically Resistant Index (VARIgreen) vegetation indices were the best predictors of phycocyanin concentration (Table 5), though these correlations may be an artifact of Chl *a* content within cyanobacterial cells, as GRRI was also closely related to Chl *a*. Several studies have utilized RGB UAS sensors for mapping coastal floating green tides (Xu et al. 2017), attached green algae (Xu et al. 2018), benthic cyanobacterial mats (Bollard-Breen et al. 2015), and nuisance filamentous green algae (Flynn and Chapra 2014). For example, Xu et al. (2018) calculated the Normalized Green-Blue Difference Index (NGBDI), Normalized Green-Red Difference Index (NGRDI), Visible Band Difference Vegetation Index (VDVI), and Excess Green Index (EXG) indices from RGB UAS imagery to identify green algae growing on rafts and found that NGRDI generated the most accurate results. These findings are consistent with our results, as of the four vegetation indices tested by Xu et al. (2018), NGRDI was closely related to both Chl *a* and phycocyanin. RGB UASs are primarily used for qualitative

Table 4. Correlation analysis between log-transformed Chl *a* concentrations ($\mu g\ L^{-1}$) and vegetation index values derived from UAS images captured with a DJI Phantom 4 integrated RGB camera, DJI Phantom 4 Pro integrated RGB camera, a MAPIR Surve3 NGB sensor, and a Parrot Sequoia multispectral sensor. $n = 70$.

	Phantom 4 RGB		Phantom 4 Pro RGB		Survey3W NGB		Parrot Sequoia multispectral	
	r^2	*p* value	r^2	*p* value	r^2	*p* value	r^2	*p* value
BNDVI	—	—	—	—	0.00	0.60	—	—
CiGreen	—	—	—	—	0.01	0.33	0.67	<0.0001
CIRedEdge	—	—	—	—	—	—	0.02	0.25
CIVE	0.31	<0.0001	0.35	<0.0001	—	—	—	—
DVI	—	—	—	—	—	—	0.76	<0.0001
ENDVI	—	—	—	—	0.02	0.22	—	—
EVI2	—	—	—	—	—	—	0.79	<0.0001
EXG	0.29	<0.0001	0.33	<0.0001	—	—	—	—
ExGR	0.11	0.006	0.06	0.04	—	—	—	—
GNDVI	—	—	—	—	0.00	0.77	0.68	<0.0001
GRRI	0.231	<0.0001	0.28	<0.0001	—	—	0.32	<0.0001
KIVU	0.01	0.32	0.08	0.02	—	—	—	—
MSR	—	—	—	—	—	—	0.75	<0.0001
MSRre	—	—	—	—	—	—	0.02	0.25
NDRE	—	—	—	—	—	—	0.02	0.27
NDVI	—	—	—	—	—	—	0.79	<0.0001
NDVSI	—	—	—	—	—	—	0.77	<0.0001
NGBDI	0.04	0.10	0.02	0.23	0.00	0.99	—	—
NGRDI	0.30	<0.0001	0.28	<0.0001	—	—	0.30	<0.0001
RGBVI	0.12	0.003	0.20	0.0001	—	—	—	—
RGRI	0.30	<0.0001	0.27	<0.0001	—	—	0.28	<0.0001
RNDVI	—	—	—	—	—	—	0.45	<0.0001
RVI	—	—	—	—	—	—	0.61	<0.0001
VARIgreen	0.31	<0.0001	0.26	<0.0001	—	—	—	—
VDVI	0.25	<0.0001	0.24	<0.0001	—	—	—	—
VEG	0.02	0.24	0.12	0.003	—	—	—	—

Table 5. Correlation analysis between log-transformed phycocyanin concentrations ($\mu g\ L^{-1}$) and vegetation index values derived from UAS images captured with a DJI Phantom 4 integrated RGB camera, DJI Phantom 4 pro integrated RGB camera, a MAPIR Surve3 NGB sensor, and a Parrot Sequoia multispectral sensor. $n = 67$.

	Phantom 4 RGB		Phantom 4 Pro RGB		Survey3W NGB		Parrot Sequoia Multispectral	
	r^2	*p* value	r^2	*p* value	r^2	*p* value	r^2	*p* value
BNDVI	—	—	—	—	0.02	0.38	—	—
CiGreen	—	—	—	—	0.01	0.56	0.64	<0.0001
CIRedEdge	—	—	—	—	—	—	0.08	0.03
CIVE	0.13	0.003	0.12	0.004	—	—	—	—
DVI	—	—	—	—	-	-	0.54	<0.0001
ENDVI	—	—	—	—	0.12	0.005	—	—
EVI2	—	—	—	—	—	—	0.60	<0.0001
EXG	0.12	0.004	0.11	0.005	—	—	—	—
ExGR	0.07	0.03	0.04	0.10	—	—		
GNDVI	—	—	—	—	0.00	0.86	0.64	<0.0001
GRRI	0.24	<0.0001	0.18	0.0003	—	—	0.12	0.001
KIVU	0.03	0.19	0.09	0.02	—	—	—	—
MSR	—	—	—	—	—	—	0.60	<0.0001
MSRre	—	—	—	—	—	—	0.08	0.03
NDRE	—	—	—	—	—	—	0.08	0.04
NDVI	—	—	—	—	—	—	0.59	<0.0001
NDVSI	—	—	—	—	—	—	0.57	<0.0001
NGBDI	0.00	0.59	0.06	0.97	0.03	0.18	—	—
NGRDI	0.21	<0.0001	0.16	0.0007	—	—	0.08	0.04
RGBVI	0.03	0.14	0.07	0.03	—	—	—	—
RGRI	0.18	0.0004	0.15	0.001	—	—	0.15	0.001
RNDVI	—	—	—	—	—	—	0.43	<0.0001
RVI	—	—	—	—	—	—	0.52	<0.0001
VARIgreen	0.21	<0.0001	0.17	0.0005	—	—	—	—
VDVI	0.10	0.008	0.09	0.01	—	—	—	—
VEG	0.01	0.33	0.07	0.03	—	—	—	—

rather than quantitative assessment of CyanoHABs, but the low cost and ease of use of RGB sensors warrants further research.

Vegetation index values generated from the modified multispectral MAPIR Survey3W NGB sensor indicate that it is not reliable for quantifying phytoplankton abundance. Of the five vegetation indices calculated, the Enhanced Normalized Difference Vegetation Index (ENDVI) was the best predictor of both Chl *a* ($r^2 = 0.02$, $p = 0.22$; Table 4) and phycocyanin ($r^2 = 0.12$, $p = 0.005$; Table 5). ENDVI was designed to inflate the Chl *a* reflection values by combining reflectance from near-infrared and green wavelengths (MaxMax 2015). Blue Normalized Vegetation Index (BNDVI) values generated from modified multispectral NGB sensors have been used for monitoring cyanobacterial buoyant packed cell volume (Van der Merwe and Price 2015). BNDVI was not significantly correlated with Chl *a* or phycocyanin in our study, potentially due to the high cyanobacterial densities in our systems, as BNDVI can become saturated and less reliable as buoyant packed cell volume increases.

Aerial images collected with the Parrot Sequoia multiband multispectral sensor generated the best estimates of Chl *a* and phycocyanin of the four sensors. Of the 15 vegetation indices calculated from multiband multispectral aerial images, Difference Vegetation Index (DVI), 2-Band Enhanced Vegetation Index (EVI2), Normalized Difference Vegetation Index (NDVI), and Normalized Difference Vegetation Structure Index (NDVSI) were highly correlated to Chl *a* concentration (Table 4). NDVI was originally developed for monitoring terrestrial vegetation using satellite remote sensors (Rouse et al. 1974). While satellite NDVI values are often distorted by atmospheric disturbances and cloud cover, UAS images are collected at a lower altitude which decreases atmospheric effects (Choo et al. 2018). Currently, NDVI is one of the most measured vegetation indices for precision agriculture, and it provided the best estimate of Chl *a* ($r^2 = 0.79$, $p < 0.0001$,

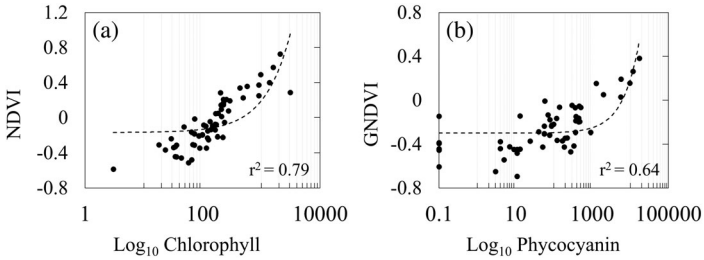

Fig 5. Correlation between log-transformed chlorophyll (**a**) and phycocyanin (**b**) concentrations (μg L^{-1}) and vegetation indices derived from UAS images captured with a Parrot Sequoia multispectral sensor.

Fig. 5) of all the sensor and vegetation index combinations in this study. Multiband multispectral aerial images also generated the best estimates of cyanobacterial abundance, with the Green Chlorophyll Index (CiGreen), Green Normalized Difference Vegetation Index (GNDVI), and NDVSI vegetation indices generating the best phycocyanin estimates of all four sensors and vegetation index combinations (Table 5; Fig. 5). The red-edge wavelength is included in many multispectral sensors because it significantly improves crop health estimates (Lu et al. 2019). However, of the 15 vegetation indices generated from the multiband multispectral sensor, vegetation indices that included the red-edge wavelength, such as the Normalized Difference Red-Edge Index (NDRE) and Modified Simple Ratio Red-Edge (MSRre), generated the least reliable estimates of Chl *a* and phycocyanin.

Many multiband multispectral sensors are specifically designed to record peak reflectance and absorbance characteristics of terrestrial Chl *a*. Vegetation indices that included the red and near-infrared wavelengths provided the best Chl *a* and phycocyanin estimates, as near-infrared wavelengths are reflected at a higher degree than green wavelengths. Studies that utilized both UAS and satellites for monitoring water quality in reservoirs also found that vegetation indices that include the red and near-infrared wavelengths, such as the Ratio Vegetation Index (RVI) and NDVI, performed the best for estimating Chl *a* (Beck et al. 2016; Cillero Castro et al. 2020). However, measuring the near-infrared wavelength did not necessarily generate more reliable results, as seen with the modified multispectral Survey3W NGB sensor. The Cigreen and GNDVI vegetation indices were both calculated from modified and multiband multispectral sensor aerial images, yet they vary greatly in their relationship to both Chl *a* and phycocyanin (Tables 4 and 5). Differences between the sensors could be attributed to the differences in wavelengths and bandwidths, as well as resolution (Table 2; Fig. 1). The Survey3W NGB records near-infrared data at the 850 nm range at a bandwidth of 30 nm, whereas the Parrot Sequoia records near-infrared at the 790 nm range at a bandwidth of 40 nm (Fig. 1). A study conducted by Lu et al. (2019) compared the ability of three-band modified multispectral, multiband multispectral, and hyperspectral sensors for estimating terrestrial crop cover and found wavelengths recorded by modified multispectral sensors generate low accuracy imagery that should be restricted to mapping rather than quantification (Lu et al. 2019). Such discrepancies were not found between vegetation index values generated from the two RGB sensors and the multiband multispectral sensors (i.e., GRRI, NGRDI, and RGRI; Tables 4 and 5). This suggests that the improved resolution of the multispectral sensor was not as important as the addition of the near-infrared band for estimating photosynthetic pigments.

Many of the vegetation indices designed for estimating algal abundance from satellite remote sensors, including the Floating Algae Index (FAI) generated from MODIS wavelengths (Hu 2009) and the Cyanobacterial Index (CI) generated from MERIS wavelengths (Wynne et al. 2010), require sensors that measure wavelengths most commercial drones are not equipped to record. Some vegetation indices, such as KIVU generated from Landsat 5 images, utilize visible wavelength data for determining Chl *a* in inland aquatic ecosystems (Brivio et al. 2001). However, KIVU was a poor measure of Chl *a* in our highly productive ponds (Table 4), likely because KIVU was generated from systems with relatively low Chl *a* concentrations (Brivio et al. 2001).

Discussion

Rapid quantitative measurements of cyanobacterial abundance are necessary for implementing timely management decisions, such as chemical treatments for aquaculture and drinking water, restricting access to recreational waterbodies, and identifying spatio-temporal patterns for forecasting. Traditional water sampling techniques provide a snapshot of cyanobacterial abundance, ecosystem conditions, and the presence of cyanotoxins but do not illustrate how the system changes spatially or temporally and can be constrained by processing times and cost. Algorithms created for satellite remote sensing data are capable of monitoring cyanobacterial abundance in large waterbodies, but the spatial resolution is not fine enough for measuring smaller systems and interpreting satellite data requires training (Kutser 2004). There are currently no commercially available UAS sensors designed specifically for aquatic ecosystem monitoring, as most sensors and vegetation indices are designed for detecting terrestrial vegetation. However, commercial sensors are easy to use, affordable, and allow rapid whole ecosystem estimates of phytoplankton abundance.

The Parrot Sequoia multiband multispectral sensor yielded the best estimates of chlorophyll and phycocyanin concentrations (Fig. 5). These results are largely attributed to the inclusion of the NIR wavelength, as chlorophyll and phycocyanin reflect NIR to a higher degree than green leading to greater spectral absorption differences (Simis and Kauko 2012). However, poor chlorophyll and phycocyanin estimates generated from the Survey3W modified multispectral sensor highlight

the importance of prioritizing measured wavelength and bandwidth over measured index (i.e., band color) when choosing a commercially available sensor. This is evident when comparing the overlap between measured indices of the Survey3W NGB and Parrot Sequoia multispectral sensors, which measured the same indices but generated different estimates (Tables 4 and 5, Fig. 1). All four sensors included in this study were more sensitive to Chl *a* concentrations than phycocyanin, likely because phycocyanin absorbs light at 620 nm, which is not measured by most commercially available sensors. Results from this study suggest multiband multispectral sensors can be utilized for estimating phytoplankton abundance, but further research should be conducted to determine whether these tools can reliably differentiate between Chl *a* and phycocyanin. While more sophisticated UAS sensors (i.e., hyperspectral) provide more reliable information of phytoplankton species composition and abundance, hyperspectral sensors are an impractical alternative for rapid detection of phytoplankton abundance due to their high cost and challenging workflow (Kislik et al. 2018). Although remote sensing imagery cannot estimate cyanotoxins (e.g., microcystin and cylindrospermopsin) or off-flavor compounds (e.g., geosmin and MIB), photosynthetic pigment estimates based on UAS images could be instrumental for early detection and management of CyanoHABs.

References

Beck, R., S. Zhan, H. Liu, and others. 2016. Comparison of satellite reflectance algorithms for estimating chlorophyll-a in a temperate reservoir using coincident hyperspectral aircraft imagery and dense coincident surface observations. Remote Sens. Environ. **178**: 15–30. doi:10.1016/j.rse.2016.03.002

Biggs, J., S. von Fumetti, and M. Kelly-Quinn. 2017. The importance of small waterbodies for biodiversity and ecosystem services: Implications for policy makers. Hydrobiologia **793**: 3–39. doi:10.1007/s10750-016-3007-0

Bollard-Breen, B., and others. 2015. Application of an unmanned aerial vehicle in spatial mapping of terrestrial biology and human disturbance in the McMurdo Dry Valleys. East Antarctica. Polar Biol. **38**: 573–578. doi:10.1007/s00300-014-1586-7

Brando, V. E., and A. G. Dekker. 2003. Satellite hyperspectral remote sensing for estimating estuarine and coastal water quality. IEEE Trans. Geosci. Remote Sens. **41**: 1378–1387. doi:10.1109/TGRS.2003.812907

Brivio, P. A., C. Giardino, and E. Zilioli. 2001. Determination of chlorophyll concentration changes in Lake Garda using an image-based radiative transfer code for Landsat TM images. Int. J. Remote Sens. **22**: 487–502. doi:10.1080/014311601450059

Cheng, K. H., S. N. Chan, and J. H. W. Lee. 2020. Remote sensing of coastal algal blooms using unmanned aerial vehicles (UAVs). Mar. Pollut. Bull. **152**: 110889. doi:10.1016/j.marpolbul.2020.110889

Choo, Y., G. Kang, D. Kim, and S. Lee. 2018. A study on the evaluation of water-bloom using image processing. Environ. Sci. Pollut. Res. **25**: 36775–36780. doi:10.1007/s11356-018-3578-6

Cillero Castro, C., J. A. Domínguez Gómez, J. Delgado Martín, B. A. Hinojo Sánchez, J. L. Cereijo Arango, F. A. Cheda Tuya, and R. Díaz-Varela. 2020. An UAV and satellite multispectral data approach to monitor water quality in small reservoirs. Remote Sensing **12**: 1514:1–33. 10.3390/rs12091514

Drozd, A., P. d. T. Pinto, V. Fernández, M. Bazzalo, F. Bordet, and G. Ibañez. 2020. Hyperspectral remote sensing monitoring of cyanobacteria blooms in a large South American reservoir: high- and medium-spatial resolution satellite algorithm simulation. Mar. Freshw. Res. **71**: 593–605. doi:10.1071/MF18429

Flynn, K. F., and S. C. Chapra. 2014. Remote sensing of submerged aquatic vegetation in a shallow non-turbid river using an unmanned aerial vehicle. Remote Sens. (Basel) **6**: 12815–12836. doi:10.3390/rs61212815

García-Fernández, M., E. Sanz-Ablanedo, and J. R. Rodríguez-Pérez. 2021. High-resolution drone-acquired RGB imagery to estimate spatial grape quality variability. Agronomy **11**: 655. doi:10.3390/agronomy11040655

Hu, C. 2009. A novel ocean color index to detect floating algae in the global oceans. Remote Sens. Environ. **113**: 2118–2129. doi:10.1016/j.rse.2009.05.012

Huisman, J., G. A. Codd, H. W. Paerl, B. W. Ibelings, J. M. H. Verspagen, and P. M. Visser. 2018. Cyanobacterial blooms. Nat. Rev. Microbiol. **16**: 471–483. doi:10.1038/s41579-018-0040-1

Kasinak, J.-M. E., B. M. Holt, M. F. Chislock, and A. E. Wilson. 2015. Benchtop fluorometry of phycocyanin as a rapid approach for estimating cyanobacterial biovolume. J. Plankton Res. **37**: 248–257. doi:10.1093/plankt/fbu096

Kataoka, T., T. Kaneko, H. Okamoto, and S. Hata. 2003. Crop growth estimation system using machine vision. *2003* IEEE/ASME International Conference on Advanced Intelligent Mechatronics (AIM 2003). IEEE: 1079–1083. doi:10.1109/AIM.2003.1225492

Kislik, C., I. Dronova, and M. Kelly. 2018. UAVs in support of algal bloom research: A review of current applications and future opportunities. Drones **2**: 35. doi:10.3390/drones2040035

Kutser, T. 2004. Quantitative detection of chlorophyll in cyanobacterial blooms by satellite remote sensing. Limnol. Oceanogr. **49**: 2179–2189. doi:10.4319/lo.2004.49.6.2179

Kutser, T., L. Metsamaa, N. Strömbeck, and E. Vahtmäe. 2006. Monitoring cyanobacterial blooms by satellite remote sensing. Estuar. Coast. Shelf Sci. **67**: 303–312. doi:10.1016/j.ecss.2005.11.024

Lomax, A. S., W. Corso, and J. F. Etro. 2005. Employing unmanned aerial vehicles (UAVs) as an element of the Integrated Ocean Observing System, p. 184–190. *In* OCEANS 2005 MTS/IEEE. Proceedings of the OCEANS 2005 MTS/IEEE, v. **1**.

Lu, B., Y. He, and P. D. Dao. 2019. Comparing the performance of multispectral and hyperspectral images for estimating vegetation properties. IEEE J. Sel. Top. Appl. Earth Obs. Remote Sens. **12**: 1784–1797. doi:10.1109/JSTARS.2019.2910558

MAPIR CAMERA. 2020. Processing Survey3 camera images. MAPIR CAMERA. https://www.mapir.camera/pages/processing-survey3-camera-images

MaxMax. 2015. Enhanced Normalized Difference Vegetation Index (ENDVI). MaxMax.com.

Merel, S., D. Walker, R. Chicana, S. Snyder, E. Baurès, and O. Thomas. 2013. State of knowledge and concerns on cyanobacterial blooms and cyanotoxins. Environ. Int. **59**: 303–327. doi:10.1016/j.envint.2013.06.013

Morel, A. 2001. Bio-optical models, p. 317–326. *In* J. H. Steele [ed.], Encyclopedia of ocean sciences. Academic Press.

Oliver, R. L., D. P. Hamilton, J. D. Brookes, and G. G. Ganf. 2012. Physiology, blooms and prediction of planktonic cyanobacteria, p. 155–194. *In* B. A. Whitton [ed.], Ecology of cyanobacteria II: Their diversity in space and time. Springer.

Ortega-Terol, D., D. Hernandez-Lopez, R. Ballesteros, and D. Gonzalez-Aguilera. 2017. Automatic hotspot and sun glint detection in UAV multispectral images. Sensors **17**: 1–16. doi:10.3390/s17102352

Rouse, W., R. H. Haas, J. A. Schell, and D. W. Deering. 1974. Monitoring vegetation systems in the Great Plains with ERTS, p. 301–317. *In* Proceedings of the Third Earth Resources Technology Satellite—1 Symposium.

Sartory, D. P., and J. U. Grobbelaar. 1984. Extraction of chlorophyll-a from freshwater phytoplankton for spectrophotometric analysis. Hydrobiologia **114**: 177–187. doi:10.1007/BF00031869

Schober, P., C. Boer, and L. A. Schwarte. 2018. Correlation coefficients: Appropriate use and interpretation. Anesth. Analg. **126**: 1763–1768. doi:10.1213/ANE.0000000000002864

Shi, K., Y. Zhang, Y. Zhou, X. Liu, G. Zhu, B. Qin, and G. Gao. 2017. Long-term MODIS observations of cyanobacterial dynamics in Lake Taihu: Responses to nutrient enrichment and meteorological factors. Sci. Rep. **7**: 1–16. doi:10.1038/srep40326

Simis, S. G. H., and H. M Kauko. 2012. In vivo mass-specific absorption spectra of phycobilipigments through selective bleaching. Limnol. Oceanogr. Methods. **10**: 214–226. doi:10.4319/lom.2012.10.214

Tucker, C. S., and K. K. Schrader. 2020. Off-flavors in pond-grown ictalurid catfish: Causes and management options. J. World Aquacult. Soc. **51**: 7–92. doi:10.1111/jwas.12672

Van der Merwe, D., and K. Price. 2015. Harmful algal bloom characterization at ultra-high spatial and temporal resolution using small unmanned aircraft systems. Toxins **7**: 1065–1078. doi:10.3390/toxins7041065

Wynne, T. T., R. P. Stumpf, M. C. Tomlinson, and J. Dyble. 2010. Characterizing a cyanobacterial bloom in Western Lake Erie using satellite imagery and meteorological data. Limnol. Oceanogr. **55**: 2025–2036. doi:10.4319/lo.2010.55.5.2025

Xu, F., Z. Gao, X. Jiang, J. Ning, X. Zheng, D. Song, J. Ai, and M. Chen. 2017. Mapping of green tide using true color aerial photographs taken from a unmanned aerial vehicle. Remote sensing and modeling of ecosystems for sustainability XIV, International Society for Optics and Photonics. 104050M. doi:10.1117/12.2271724

Xu, F., Z. Gao, X. Jiang, W. Shang, J. Ning, D. Song, and J. Ai. 2018. A UAV and S2A data-based estimation of the initial biomass of green algae in the South Yellow Sea. Mar. Pollut. Bull. **128**: 408–414. doi:10.1016/j.marpolbul.2018.01.061

Xue, J., and B. Su. 2017. Significant remote sensing vegetation indices: A review of developments and applications. J. Sens. **2017**: e1353691. doi:10.1155/2017/1353691, 1, 17

Yacobi, Y. Z., W. J. Moses, S. Kaganovsky, B. Sulimani, B. C. Leavitt, and A. A. Gitelson. 2011. NIR-red reflectance-based algorithms for chlorophyll-a estimation in mesotrophic inland and coastal waters: Lake Kinneret case study. Water Res. **45**: 2428–2436. doi:10.1016/j.watres.2011.02.002

Acknowledgments

We would like to thank two anonymous reviewers for suggestions that improved an earlier version of the manuscript. We appreciate the help of Evann Martin and members of the WilsonLab at Auburn University for assisting with sample collection and processing. We thank the Jule Collins Smith Museum and E. W. Shell Fisheries Center at Auburn University and the owners and operators of the commercial aquaculture facility for allowing us to collect data at their facilities. This study was supported by the NSF Graduate Research Fellowship Program, USDA grants 2017-70007-27132 and 58-6010-0-006, the Alabama Agricultural Experiment Station, and the Hatch program (ALA016-1-16007) of the National Institute of Food and Agriculture, U.S. Department of Agriculture.

Submitted 30 March 2021
Revised 05 November 2021
Accepted 30 November 2021

Associate editor: Ivona Cetinic